

# Spatio-temporal Proper Orthogonal Decomposition of turbulent channel flow

Srikanth Derebail Muralidhar<sup>1</sup>, Bérengère Podvin<sup>1†</sup>,  
Lionel Mathelin<sup>1,2</sup> and Yann Fraigneau<sup>1</sup>

<sup>1</sup>LIMSI, CNRS, Université Paris-Saclay, 91403 Orsay Cedex, France

<sup>2</sup>Dpt. Applied Mathematics, Univ. Washington, Seattle, WA, USA

(Received xx; revised xx; accepted xx)

An extension of Proper Orthogonal Decomposition is applied to the wall layer of a turbulent channel flow ( $Re_\tau = 590$ ), so that empirical eigenfunctions are defined in both space and time. Due to the statistical symmetries of the flow, the eigenfunctions are associated with individual wavenumbers and frequencies. Self-similarity of the dominant eigenfunctions, consistent with wall-attached structures transferring energy into the core region, is established. The most energetic modes are characterized by a fundamental time scale in the range 200-300 viscous wall units. The full spatio-temporal decomposition provides a natural measure of the convection velocity of structures, with a characteristic value of  $12u_\tau$  in the wall layer. Finally, we show that the energy budget can be split into specific contributions for each mode and provides a new closure formulation for the quadratic terms.

**Key words:**

## 1. Introduction

Proper Orthogonal Decomposition (POD) was first introduced in turbulence by Lumley (1967). Its derivation stemmed from the Karhunen-Loève (KL) decomposition (Loève 1977) which represents a square-integrable centered stochastic process in the time domain  $U(t)$  as an infinite linear combination of orthogonal functions. If  $t$  is defined over a finite range, then

$$U(t) = \sum_n a^n \chi^n(t), \quad (1.1)$$

where  $a^n$  is stochastic and  $\chi^n$  are continuous functions. It is important to note that  $U(t)$  represents a stochastic variable and not a sample. Realizations of  $U(t)$  will be noted  $u(t)$ . The functions  $\chi^n(t)$  are the eigenfunctions of the covariance function  $K_U(t, t') = \mathbb{E}[U_t U_{t'}]$ , where the operator  $\mathbb{E}$  refers to expectation with respect to the measure of  $U$ . In the Karhunen-Loève derivation, the variable  $t$  corresponds to time, but it could indicate any other variable - such as space.

Lumley (1967) adapted the decomposition to Fluid Mechanics: the samples were constituted by flow realizations, and the ergodicity assumption was used to replace the covariance function corresponding to an ensemble average with one obtained by the time average so that the KL transform was generally applied to space. He considered

† Email address for correspondence: Berengere.Podvin@limsi.fr

the spatial autocorrelation tensor  $K_U(x, x') = \langle U(x, t)U(x', t) \rangle$ , where now  $x$  and  $x'$  represent the deterministic variable (space) and  $\langle \cdot \rangle$  represents the ensemble average (which is simply the time average here).  $K_U(x, x')$  therefore represents the spatial autocorrelation tensor at zero time lag. As pointed out by George (2017), it is important to realize that the spatial auto-correlation tensor  $K_U(x, x')$  is different from its sampled estimation  $\frac{1}{N_s} \sum_{i=1}^{N_s} u(x, t^i)u(x', t^i)$ , where  $N_s$  is the number of samples. In general, exact eigenfunctions of  $K_U(x, x')$  cannot be computed since the  $K_U(x, x')$  can only be approximated. However, for spatially homogeneous flows such as the channel flow in horizontal directions (Aubry *et al.* 1988), exact solutions are known *a priori* since POD modes are Fourier modes in the homogeneous directions.

A key insight stated by George (2017) is that if the process is stationary in time, the KL or POD modes are Fourier modes in the deterministic variable  $t$ . Combining Fourier transform in time with Proper Orthogonal Decomposition in space was first applied in experimental studies of free turbulent shear flows, such as mixing layers and jets. Spatial and frequency decomposition was performed in the pioneering work of Glauser *et al.* (1983), Glauser & George (1987) as well as in Arndt *et al.* (1997), Delville *et al.* (1999), Citriniti & George (2000), Ukeiley *et al.* (2001). However, as far as we know, a full four-dimensional decomposition was never attempted for any flow until recently (see the spectral POD of Towne *et al.* (2018)), and has never been implemented for wall-bounded flows. The present work builds on these previous developments, and implements George’s suggestion to apply the decomposition in the four-dimensional space, i.e., in both time and space, reverting to ensemble average (as in the original definition) to evaluate the covariance function. This will allow us to identify modes that can be associated with individual spatial wavenumbers and temporal frequencies. Such decompositions could be useful to identify key features and instability mechanisms underlying the flow dynamics and eventually attempt to control them. One particularly promising approach for this is the resolvent analysis (McKeon 2017), which is based on the Navier-Stokes equations. In contrast, the present approach is data-based, and can therefore provide a complementary viewpoint.

As mentioned above, we note that another four-dimensional decomposition is provided by the Spectral POD introduced by Towne *et al.* (2018). Their method only requires stationarity in time, so that temporal Fourier transform can be applied, while standard snapshot POD is performed in the spatial directions. In contrast, in our implementation, we apply Fourier transform in the spatial (horizontal) directions where turbulence is homogeneous. The connection of the present method with the snapshot POD and the dynamic mode decomposition (DMD) is discussed in Section 3.

In the present paper, we apply fully spatio-temporal Proper Orthogonal Decomposition to the turbulent channel flow. Wall turbulence is characterized by a variety of spatio-temporal scales interacting in a highly complex fashion (Robinson 1991; Dennis 2015). It is well known that the flow is characterized by an alternation of high and low-speed streaks aligned with the flow, with a typical spacing  $\lambda_{z+} \sim 100 - 150$  in the spanwise direction and a length of  $600 - 1000$  wall units (Kim *et al.* (1971), Stanislas *et al.* (2008), Jiménez (2013)), which are units based on the fluid viscosity and wall-friction velocity  $u_\tau$ , and will be denoted with a  $+$  throughout the paper. These streaks are associated with longitudinal vortical structures pushing low-speed fluid upwards and bringing high-speed fluid downwards, which results in a strong contribution to the Reynolds stress (Kim *et al.* 1971). This contribution is highly intermittent in space and time, with ‘bursts’ of turbulence production. The time scale of the bursts is difficult to assess. Eulerian measures of the bursts yield time scales on the order of 300 wall units

(Blackwelder & Haritodinis 1983). This value is based on the VITA (Variable Interval Time Average) criterion applied to the streamwise velocity and depends on the choice of a particular threshold, which makes it difficult to provide an absolute value for the bursting period. However the value appears to be independent of the Reynolds number. Minimal flow units, i.e., periodic domains of small extent (Jiménez 2013) were characterized by global characteristic time scales of 300-400 wall units, which appear to correspond to regeneration cycles of coherent structures (Hamilton *et al.* 1995), but relating this time scale with that of a full-scale turbulent flow is difficult.

Classic spatial POD has been previously used to investigate the boundary layer (e.g., see Aubry *et al.* (1988), Moin & Moser (1989), Podvin & Lumley (1998)). Spatial eigenfunctions are determined from second-order statistics. The amplitudes of eigenfunctions are characterized by a mixture of time scales and can only be computed by projecting the full instantaneous field onto the spatial eigenfunctions. In contrast, the new decomposition directly provides spatio-temporal patterns.

In this paper we focus on a relatively moderate Reynolds number  $Re_\tau = 590$ , based on the fluid viscosity, channel half-height and friction velocity. At these moderate Reynolds numbers our focus will be on the wall layer as large scales such as those observed by Smits *et al.* (2011) are not present in the flow. The rest of the paper is organized in the following manner. Section 2 gives details of the methodology for the spatio-temporal POD. Section 3 presents the POD results. The contributions to the turbulent kinetic energy equation associated with each mode are examined in Section 4, followed by a conclusion in Section 5 which summarizes the key observations and results.

## 2. Description of the procedure

### 2.1. Full spatio-temporal POD

Owing to the homogeneity of the statistics in the spatial directions  $x$  and  $z$  and their stationarity, POD modes are Fourier modes in the horizontal directions as well as in time. Here, for each configuration, the Fourier transform of the velocity is computed in the temporal and the homogeneous spatial directions for each sample corresponding to a set of fields. The  $p$ th component of the velocity field ( $u^p(x, y, z, t)$ ) in the physical space is then written as

$$u^p(x, y, z, t) = \sum_l \sum_k \sum_f u_{lkf}^p(y) e^{2\pi i(lx/L_x + kz/L_z + ft/T)}, \quad (2.1)$$

where  $u_{lkf}^p(y)$  denotes the  $p$ th velocity component in the Fourier space corresponding to the streamwise wavenumber  $l$ , spanwise wavenumber  $k$  and frequency  $f$ . Proper Orthogonal Decomposition is then applied in the wall-normal direction for each triad  $(l, k, f)$ :

$$u_{lkf}^p(y) = \sum_n a_{lkf}^n \phi_{lkf}^{n,p}(y), \quad (2.2)$$

with, for any 4-uplet  $(l, k, f, n)$ ,

$$\langle a_{lkf}^n a_{lkf}^{*m} \rangle = \delta_{mn} \lambda_{lkf}^n. \quad (2.3)$$

Here,  $\langle \cdot \rangle$  represents the usual ensemble average over the space of all possible flow realizations,  $\delta_{mn}$  is the Kronecker-delta function,  $n$  denotes a specific POD mode for each triad, and  $*$  denotes complex conjugation. Note that  $a_{lkf}^n$  is independent of  $p$  as the three velocity components are stacked into a single vector. The complex, stochastic coefficients  $a_{lkf}^n$  are uncorrelated and their variance is equal to  $\lambda_{lkf}^n$ .

The eigenfunctions  $\phi_{lkf}^{n,p}$  and eigenvalues  $\lambda_{lkf}^n$  are obtained by solving the following eigenproblem, where the autocorrelation is estimated from taking an ensemble average:

$$\int_0^Y \langle \mathbf{u}_{lkf}(y) \mathbf{u}_{lkf}^*(y') \rangle \phi_{lkf}^n(y') dy' = \lambda_{lkf}^n \phi_{lkf}^n(y). \quad (2.4)$$

Here,  $\mathbf{u}_{lkf}(y)$  represents the single velocity vector with the three components stacked in it. Upon discretization in  $y$ ,  $\phi_{lkf}^n(y)$  represents the single eigenvector containing the three components. By construction, the eigenvectors are orthogonal with respect to the Euclidean inner product, and  $\lambda_{lkf}^n$  can be interpreted as the energy content in each mode. Similarly, for each triad  $(l, k, f)$ , the modes (i.e., different  $n$ 's) are sorted by energy. Since the left-hand-side of Equation (2.4) is a Hilbert-Schmidt integral operator, its eigenvalues are real and non-negative. The eigenvalues  $\lambda_{lkf}^n$  associated to the triplets  $(l, k, f)$  can then be gathered and sorted globally according to their magnitude. We will call *mode number* the global index  $N(l, k, f, n)$  associated with the sorted modes over spatial wavenumbers  $(l, k)$ , frequency  $(f)$  and quantum number  $n$ , with lower *mode number* indicating a larger eigenvalue. In all that follows, we focus only on the most energetic modes.

## 2.2. Numerical implementation

The methodology is summarized in Figure 1. Since POD is also applied in time, the autocorrelation tensor needs to be computed from several independent realizations of the same experiment. An ideal sample would consist of the Fourier transform in space and time of the velocity field corresponding to different databases obtained at the same Reynolds number. In practice, owing to the cost of the simulation, we split a single database into several contiguous chunks of length  $T$ , each of which constitutes a sample. The samples are therefore not independent realizations, but we assume that the period  $T$  is sufficiently larger than the characteristic time scales of the flow, or at least sufficiently large to allow separation of the dominant time scales. Yet  $T$  cannot be too large in order to allow for a reasonable number of samples  $N_s$  to be constituted. We note that as in Moin & Moser (1989) and Podvin (2001), the number of samples is doubled by considering spanwise reflections and quadrupled by considering both lower and upper parts of the channel (including spanwise reflections).

Each sample then consists of a block of  $n_t$  velocity fields uniformly sampled at a rate  $\delta t$ . The value of  $\delta t$  is chosen such that the Nyquist frequency is well above the range of characteristic frequencies of the flow. It is however limited by computational tractability, as larger  $n_t$  leads to a larger size of sample thereby increasing memory requirements. For most of the test cases, we have fixed the value of  $T$  to be 3000 wall units.

We use the finite-volume code SUNFLUIDH to simulate the incompressible flow in a channel. Further details on the configuration and numerical scheme can be found in Podvin & Fraigneau (2014). Periodic boundary conditions are enforced in the streamwise ( $x$ ) and the spanwise direction ( $z$ ), and the channel lengths along these directions are  $L_x = 2\pi h$  and  $L_z = \pi h$ , where  $h$  is the channel half-height. The total domain is discretized using a grid of size  $256 \times 256 \times 256$ , with a uniform grid for the horizontal directions  $x$  and  $z$  and a hyperbolic tangent-distributed mesh for the wall-normal direction  $y$ . The velocity components in the streamwise, wall-normal and spanwise direction will be denoted respectively by  $u, v, w$  or equivalently by  $u_1, u_2, u_3$ . The simulation is conducted at  $\text{Re}_\tau = 590$ , based on the friction velocity  $u_\tau$  and channel half-height  $h$ , which corresponds to the simulation of Moser *et al.* (1999). The database consists of 16500 flow realizations, separated by  $\delta t_+ = 5.9$ . The time spanned by the database represents about  $10^5$  viscous time units.

In most of the paper, we focus on the domain  $y_+ < Y_+ = 80$ , but we also considered

Name	$L_x/h$	$L_z/h$	$Y/h$	$n_t$	$N_s$	$\delta t_+$	$T_+$
D1	$\pi/2$	$\pi$	0.14	100	60	29.5	2950
D2	$\pi/2$	$\pi$	0.14	100	120	29.5	2950
D3	$\pi/2$	$\pi$	0.14	500	132	5.9	2950
D4	$\pi/2$	$\pi$	1	500	132	5.9	2950

Table 1: Description of different test cases;  $n_t$  denotes the number of snapshots in a given block,  $N_s$  denotes the number of samples,  $\delta t_+$  is the time gap between successive snapshots, and  $T_+$  is the total time period for a given block (expressed in viscous units).

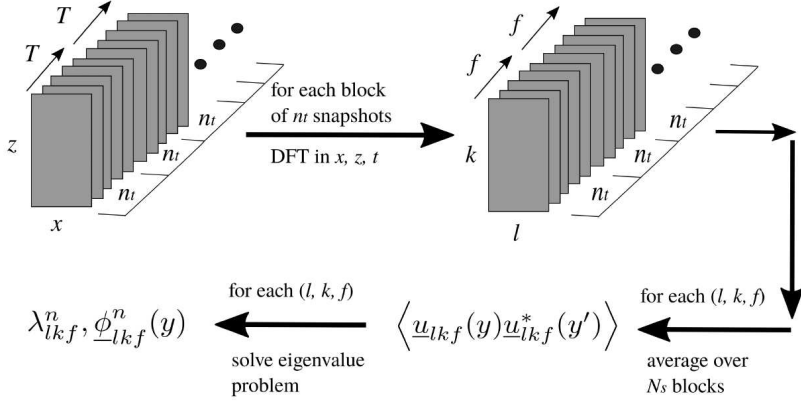


Figure 1: Schematic of the methodology. Each grey slab on the left represents an instantaneous realization of the flow in the physical domain (the wall-normal direction corresponding to the thickness of the slab), while each slab on the right corresponds to the Fourier transform of a block of  $n_t$  realizations in time as well as in the horizontal directions  $x$  and  $z$ . For each Fourier triad  $(l, k, f)$  the autocorrelation tensor is computed by averaging over the  $N_s$  blocks and an independent eigenproblem is solved.

the full boundary layer where  $Y_+ = 590$ . Due to the strong decrease of the energy spectra with the streamwise wavenumber, and given the typical extent of longitudinal streaks in the wall layer (about 600-1000 wall units (Jiménez 2013)), the streamwise extent of the domain was limited to  $L_x = \pi/2h$  representing 900 wall units. The full spanwise extent of the domain (about 1800 wall units) was considered.

Results are reported for four datasets extracted from the single database, which represent different domain sizes and sampling rates. The characteristics of the different configurations are given in Table 1. The sampling rate and number of samples were varied in the configurations D1-D3. These datasets correspond to the wall layer,  $Y_+ = 80$ . The fourth one (D4) corresponds to the full boundary-layer height,  $Y_+ = 590$ .

### 2.3. Requirements and cost of the decomposition

The spatio-temporal POD discussed in this paper relies on the same information as alternative methods such as the snapshot POD or the DMD that will be discussed in the next section. Owing to the DFT in time and homogeneous spatial directions, it however involves distinctive differences such as the requirement of collecting time-resolved snapshots, uniformly sampled in time and space. This is in contrast with the

other methods which only require time-sampling in pairs (DMD) or a set of snapshots sampled in time according to an approximately ergodic measure (snapshot POD).

Obtaining time-resolved data in the full spatial domain from a numerical simulation is not a problem, but requires integration over a sufficiently long period of time, especially if it needs to be broken down into different samples. In contrast, in an experiment, obtaining different samples over relatively long periods of time is relatively easy, but access to full spatial resolution may be more difficult, especially for time-resolved data, despite recent advances in PIV techniques (see for instance [Westerwheel \*et al.\* \(2013\)](#)). However, it should be borne in mind that ensemble average and Fourier transform commute, so that full information in the spatial domain does not have to be acquired simultaneously, since the autocorrelation tensor for given spatial separations in homogeneous directions can be computed independently. If there is one homogeneous direction (say  $x$ ), the autocorrelation tensor  $K_U(x_1, y_1, x_2, y_2) = f(x_2 - x_1, y, y')$  can be evaluated independently for each separation  $x_2 - x_1$  from two simultaneous planes  $x = x_1$  and  $x = x_2$ : the information does not have to be acquired for all positions  $x$  at the same time, only pairs of simultaneous positions are necessary. For the same reason, in the case of two homogeneous directions ( $x$  and  $z$ ), one can show that the full spatial autocorrelation tensor at all separations  $(x_1 - x_2, y_1 - y_2)$  can be entirely recovered from two orthogonal planes  $x = \text{cst}$  and  $z = \text{cst}$  (as was done in the WALLTURB experiment [Stanislas \*et al.\* \(2011\)](#)).

As mentioned above, the data is typically uniformly sampled in the homogeneous dimensions. The Fourier modes resulting from the DFT are bounded in frequency by the span of the dataset and the minimal resolution. At the price of a higher computational cost, it is however possible to overcome these limitations, if necessary. Under mild assumptions, arbitrary sampling distribution can be accounted for by reformulating the DFT as an optimization problem. Specifically, let  $\mathbf{y} \in \mathbb{R}^{n_t}$ ,  $\mathbf{y}_j \equiv y(t_j)$ , be the collection of samples in an homogeneous dimension,  $\Phi \in \mathbb{R}^{n_t \times n_c}$ ,  $\Phi_{j,k} = \exp(2\pi i k t_j / T)$ , the evaluation of the Fourier basis at the sampling points and  $\mathbf{c} = (c_1 \dots c_{n_c})^\top$  the complex-valued vector of Fourier coefficients. The DFT then amounts to solving the following optimization problem:

$$\mathbf{c} \in \arg \min_{\tilde{\mathbf{c}} \in \mathbb{C}^{n_c}} \|\mathbf{y} - \Phi \tilde{\mathbf{c}}\|, \quad n_c = n_t.$$

The retained norm is typically  $L^2$  and a closed-form solution is obtained directly via  $\mathbf{c} = \Phi^+ \mathbf{y}$ , with the superscript  $+$  denoting the Moore-Penrose pseudo-inverse. Only mild limitations apply on  $\Phi$  and general sampling schemes can be used.

If the data can be compressed in the Fourier basis (i.e., only a few modes are dominant), sub-Nyquist sampling is possible and a broader bandwidth can be obtained. Among various approaches, the compressed sensing theory offers a firm theoretical ground for this situation, see [Foucart & Rauhut \(2013\)](#) for a gentle introduction to the field. The problem can most simply be addressed by a Basis Pursuit Denoising (BPDN) formulation or with an  $L^1$ -regularization term and the LASSO algorithm ([Tibshirani 1996](#)):

$$\mathbf{c} \in \arg \min_{\tilde{\mathbf{c}} \in \mathbb{C}^{n_c}} \|\mathbf{y} - \Phi^{\text{ext}} \tilde{\mathbf{c}}\|_2^2 + \eta \|\tilde{\mathbf{c}}\|_1, \quad n_c > n_t, \quad \eta > 0, \quad (2.5)$$

where, compared to  $\Phi$ , the Fourier matrix  $\Phi^{\text{ext}}$  is enriched with basis elements of frequency higher than the highest sampling frequency. Under certain conditions on  $\Phi^{\text{ext}}$ , recovery of the Fourier coefficients  $\mathbf{c}$  is possible if the data  $\mathbf{y}$  can be expressed with a few modes in the retained Fourier basis.

We now briefly discuss the numerical cost of the solution method presented in this paper. We consider the common situation where the sampling is uniform in time and sufficient finely resolved with respect to the finest scales one is interested in. A Discrete

Fourier Transform is then applied in homogeneous dimensions. We use a multidimensional Fast Fourier Transform (FFT) which essentially amounts to the composition of a sequence of one-dimensional FFTs along each homogeneous dimension. The numerical cost of this step then retains the  $O(N \log(N))$  scaling of FFT techniques, where  $N$  is here  $N_l, N_k$  or  $n_t$ . In case of non-uniform sampling, a BPDN or LASSO formulation can be considered and efficient algorithms exist to solve the associated quadratic program (2.5). The remaining step involves a POD in the non-homogeneous dimension for each atom of triad  $(l, k, f)$ . In the present case, it then reduces to a set of *independent* one-dimensional PODs.

Finally, we would like to stress that eigenvalue problems involved in every method discussed here (spatio-temporal POD, spatial POD, DMD) can be advantageously solved by recent numerical techniques. In particular, sketching and randomized methods (Halko *et al.* 2011; Kannan & Vempala 2017) can very significantly alleviate the numerical cost and the memory requirement in cases only part of the spectrum is required, as is often the case in our applications.

### 3. Connections with alternative decomposition methods

We now briefly discuss the connection of the spatio-temporal POD with the snapshot POD and the Dynamic Mode Decomposition, two established methods for representing and analyzing fluid flows.

#### 3.1. Snapshot POD

Snapshot POD (Sirovich 1987) relies on an ergodicity assumption to identify the ensemble average operator  $\langle \cdot \rangle$  with the time-average. In practice, one has to rely on a finite set of samples (snapshots) and the average operator reduces to an empirical algebraic average. Snapshot POD then considers the empirical spatial autocorrelation tensor  $K_U(\mathbf{x}, \mathbf{x}') = n_t^{-1} \sum_{j=1}^{n_t} u(\mathbf{x}, t_j) u(\mathbf{x}', t_j)$ , with  $\mathbf{x}$  the vector-valued space variable. Autocorrelation tensor eigenfunctions  $\phi_j(\mathbf{x})$ , associated with the largest eigenvalues  $\lambda_j$ , are the dominant POD modes. The operator involved in the Fredholm equation of the snapshot POD method being Hilbert-Schmidt, its eigenfunctions are orthonormal with respect to the retained inner product, usually chosen as (unweighted) Euclidean,  $\phi_i^\top \phi_j = \delta_{ij}$ .

The spatial autocorrelation tensor  $K_U$  is estimated from a finite set of samples and then only provides an approximation of the true autocorrelation tensor  $K_U^*(\mathbf{x}, \mathbf{x}') \in \lim_{|\Omega_t| \rightarrow \infty} |\Omega_t|^{-1} \int_{\Omega_t} u(\mathbf{x}, t) u(\mathbf{x}', t) dt$ . In general, the spatial POD modes are then only an approximation of the true autocorrelation eigenvectors. In the spatio-temporal POD approach, we take advantage of the closed-form solution of the Fredholm equation in homogeneous dimensions. No approximation is then introduced and the spatio-temporal modes are the exact eigenvectors of the autocorrelation tensor along the homogeneous dimensions.

From a dynamical perspective, the temporal evolution of snapshot POD mode  $j$  is given by the orthogonal projection of the flow field onto the corresponding eigenfunction:  $a_j(t) = \phi_j^\top \mathbf{u}(t)$ , where  $\mathbf{u}(t) \equiv u(\mathbf{x}, t)$ . The time evolution of mode  $j$  then inherits many properties of the flow field such as its wide frequency content. It is important to note that, since it results from a projection, there is no guarantee that the dynamics of a snapshot POD mode is smooth in time.

In contrast, the present spatio-temporal POD relies on a spectral decomposition in the homogeneous dimensions, including time. Each mode then follows a smooth (harmonic) dynamics. The original flow field being approximated by a finite linear combination of

smooth modes, it remains smooth in time. More generally, spatio-temporal POD enjoys structure in both time and homogeneous dimensions and allows to interpret modes as coherent structures, localized in the frequency-spatial wavenumber space. In contrast, snapshot POD only enjoys structure in space and lacks structure in time, preventing identification of its modes with coherent structures the dynamics of which is essentially smooth.

### 3.2. DMD

The Dynamic Mode Decomposition (DMD) is another popular method for modal decomposition of fluid flows. Different definitions have been considered in the literature but we here focus on the original formulation discussed in Schmid (2010). Considering the flow field at a collection of  $N_x$  points in space as a vector-valued observable, and assuming it is a state vector for the underlying physical system, the DMD can be closely related to the Koopman theory, Mezić (2005); Rowley *et al.* (2009). In a nutshell, the DMD estimates the eigenvectors and associated eigenvalues of the linear operator mapping the discrete flow field at a given time to a subsequent time  $\Delta t$  in the future. Specifically,  $n_t$  time-ordered snapshots of the flow field sampled every  $\Delta t$  in time are collected in a matrix  $U$ . Each snapshot is of size  $N_x$  and constitutes a vector-valued observable  $\mathbf{u}$  of the state vector of the underlying physical system. Letting  $U_1$  be the first  $n_t - 1$  columns of  $U$  and  $U_2$  the last  $n_t - 1$  columns, the DMD is concerned with the characterization of the linear operator  $A$  such that  $U_2 \simeq A U_1$ . Formulating the approximation as an optimization problem, the eigendecomposition of the matrix  $A$  can be obtained:  $A \Psi = \Psi \Lambda$ , with  $\Psi \in \mathbb{C}^{(n_t-1) \times (n_t-1)}$  the matrix of eigenvectors and  $\Lambda \in \mathbb{C}^{(n_t-1) \times (n_t-1)}$  the diagonal matrix of eigenvalues  $\lambda_j$ . The flow field  $u(\mathbf{x}, t)$  is identified with  $\mathbf{u}(t)$  and can then be approximated at a time  $t + l \Delta t$  as

$$\mathbf{u}(t + l \Delta t) \approx \Psi \operatorname{diag}(\Psi^{-1} \mathbf{u}(t)) \boldsymbol{\lambda}^l = \Xi \boldsymbol{\lambda}^l, \quad \forall l \in \mathbb{Z},$$

where  $\boldsymbol{\lambda}^l = (\lambda_1^l \lambda_2^l \dots \lambda_{n_t-1}^l)^\top$  and the matrix  $\Xi = (\boldsymbol{\xi}_1 \boldsymbol{\xi}_2 \dots \boldsymbol{\xi}_{n_t-1})$  contains the so-called *DMD modes*  $\boldsymbol{\xi}_j$ .

Assuming the collection of snapshots is linearly independent and subtracting the empirical algebraic time-average from the snapshot data  $U$ , the DMD is equivalent to the temporal Discrete Fourier Transform (DFT), Chen *et al.* (2012). Specifically, denoting zero-mean quantities with a superscript  $\odot$ , the vector-valued observable  $\mathbf{u}^\odot(t + l \Delta t)$  then obeys

$$\mathbf{u}^\odot(t + l \Delta t) = \sum_{j=1}^{n_t-1} \exp\left(\frac{2\pi i l j}{n_t}\right) \boldsymbol{\xi}_j.$$

In this context, DMD decomposes the flow field in monochromatic spatial modes  $\boldsymbol{\xi}_j$  oscillating at a given frequency  $j/(\Delta t n_t)$  in time. Both the spatio-temporal POD and DMD then derive modes oscillating at a given frequency. The sampling frequency being a multiple integer of these frequencies, both methods represent the data with modes at the *same frequencies*.

However, an essential difference between DMD and POD is that there is no notion of ensemble average in DMD (only one sample, corresponding to the set of snapshots, is considered), and DMD modes are extracted from mapping one snapshot in the time series to the next one. Classic DMD is applied to one flow realization, and thus a mode computed at given frequency will have statistical variability over a set of realizations. In contrast, in the present decomposition, ensemble average is a key feature of the procedure and requires several samples. POD modes are extracted from the autocorrelation tensor

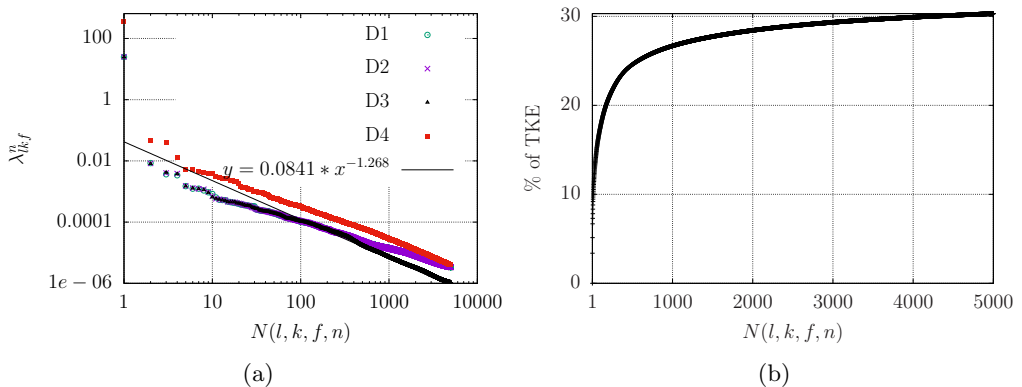


Figure 2: a) Log-log plot of the top 5000 eigenvalues for D1-D4 configurations. An asymptotic fit for the decay rate of the spectra for D3 is also shown. b) Percentage of turbulent kinetic energy (TKE) captured by the  $N$  most energetic modes for D3.

built from the different samples. They constitute an optimal basis that account for the variability of modes over an ensemble of realizations. We point out that in our numerical implementation, the different samples are obtained by breaking down a single series of snapshots into different non-overlapping blocks. We note that the connection of DMD and snapshot POD with a POD involving Fourier transform in time is also discussed in Towne *et al.* (2018) who have introduced a method called spectral POD, which also has many similarities with our present implementation. However they use the method of snapshots for all the spatial variables, whereas we apply Fourier transform in the two homogeneous spatial directions and use the direct POD method in the remaining inhomogeneous direction.

## 4. Results from spatio-temporal POD

### 4.1. POD eigenvalues

Figure 2a shows the top 5000 eigenvalues for each configuration. We note that this represents a tiny fraction of the total number of eigenvalues defined in the spatio-temporal space, which is  $3n_t \times N_l \times N_k \times N_y$ , where  $n_t$  is the number of instantaneous fields contained in a sample,  $N_l$  and  $N_k$  are respectively the numbers of streamwise and spanwise wavenumbers, and  $N_y$  is the number of grid points in the wall-normal direction. For D3 this corresponds to about  $4 \times 10^8$  degrees of freedom. The largest eigenvalue  $N(l, k, f, n) = 1$  where  $l = k = f = 0$  and  $n = 1$  corresponds to that of the mean mode (discussed in the next section). For each configuration, we have applied spatio-temporal POD to the data without removing the sample mean and compared the results to the case where the sample mean was removed. In both cases the eigenvalue distribution was very similar, and the deviations in eigenfunctions were negligibly small at least for the most energetic modes. In the rest of the paper we will focus on the  $n = 1$  eigenfunctions. We note that the eigenfunctions corresponding to  $n = 1$  capture about 80% of the turbulent kinetic energy, which is in agreement with Moin & Moser (1989)'s results.

Figure 2a shows that the spectra in D1 and D2, which correspond to a different number of samples, are essentially indistinguishable from each other. This indicates that the number of samples of ensemble averaging appears to be sufficient for the convergence of

---

Number of eigenvalues ( $N$ )	% of TKE (D3)	% of TKE (D4)
200	21	24
3000	31	33
5000	32	34

---

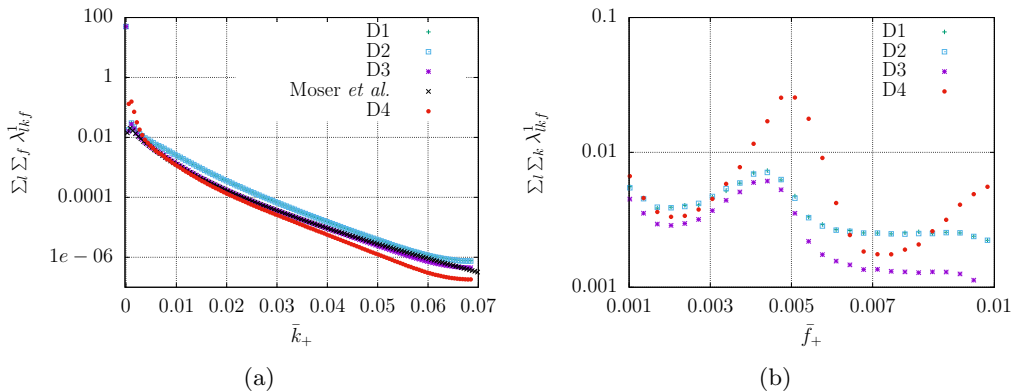
Table 2: Percentage of TKE in the first  $N$  eigenvalues for D3 and D4 configurations.

Figure 3: a) Energy spectrum ( $\sum_l \sum_f \lambda_{lkf}^1$ ) as a function of  $\bar{k}_+$ ; the data is compared with Moser *et al.* (1999)'s energy spectrum at  $y_+ = 80$  (with appropriate rescaling). b) Energy spectrum ( $\sum_l \sum_k \lambda_{lkf}^1$ ) as a function of  $\bar{f}_+$  for  $0 < y_+ < 80$  (D1-D4).

the dominant eigenvalues. The spectra in D1 and D2 are similar to that in D3 at low values of  $N$ , but have higher energy levels at large values of  $N$ , which is likely to be due to aliasing effects as the fields are sampled at higher rates there than in D3. The spectrum has an asymptotic decay of  $\lambda(N) \sim N^{-1.27}$ . Unlike the other configurations, D4 corresponds to the full boundary layer  $0 < y_+ < 590$ . As expected, energy levels are higher but the shape of the spectrum and its asymptotic decay rate are the same as in the wall region  $0 < y_+ < 80$ , which suggests self-similarity (see next section). Figure 2b shows the fraction of turbulent kinetic energy (TKE) captured by the first  $N$  modes for each  $N$  (as we are considering fluctuations, the contribution from the mean mode was set to zero). The fraction of TKE captured by the most energetic 100 mode numbers is relatively high, but increases only slightly for mode numbers higher than 1000, which highlights the complexity of the flow. The slow convergence in Fourier space also indicates that the structures are highly localized in space and time, owing to the fundamentally intermittent nature of turbulence (Frisch 1995). This is confirmed by Table 2, which shows that the first 200 eigenvalues capture about 21% of the TKE which is increased only to 32% when 5000 modes are included, for the D3 configuration. The trend remains the same for the D4 configuration, where 200 eigenvalues capture around 24% of TKE which increases only to 34% when 5000 eigenvalues are included.

Figure 3 shows the dependence of the integrated spectra with respect to the frequency and spanwise wavenumber for the different configurations. For the D3 configuration, the spatial wavenumbers and the frequency ( $\bar{l}, \bar{k}, \bar{f}$ ), expressed in wall units, are related to the mode indices  $(l, k, f)$  as

$$\bar{l}_+ = \frac{l}{927.142}, \quad \bar{k}_+ = \frac{k}{1854.286}, \quad \bar{f}_+ = \frac{f}{2950}. \quad (4.1)$$

Figure 3a shows how the sum of the eigenvalues over streamwise wavenumber and frequencies ( $\sum_l \sum_f \lambda_{l k f}^1$ ) varies as a function of  $\bar{k}_+$ . Results show a good agreement with the rescaled standard energy spectrum obtained by Moser *et al.* (1999) at  $y_+ = 80$ . As expected, the spanwise spectrum over the full layer has more energy in the lower wavenumbers and less energy at higher wavenumbers compared to that in the wall layer.

Figure 3b shows the sum of the dominant  $n = 1$  eigenvalues over all  $(l, k)$  modes (i.e.,  $\sum_l \sum_k \lambda_{l k f}^1$ ) as a function of frequency  $\bar{f}_+$  for the different configurations D1-D4. As observed previously, aliasing effects can be observed for the fields sampled in time at a lower rate (D1-D2), but the trends are very similar. A marked increase in the energy is observed in the frequency range of 0.003 – 0.005, which corresponds to time scales of 200-300 viscous units. This value is in good agreement with the duration of the regeneration cycle identified by Hamilton *et al.* (1995) and Jimenez & Moin (1991) in minimal domains, as well as the investigations of larger-scale domains reported in Jiménez (2013). A similar frequency peak is observed in the full boundary layer (D4), but with a shift towards slightly higher frequencies: the maximum is located at  $\bar{f}_+ = 0.005$ , while it is located at  $\bar{f}_+ = 0.0044$ , in the region  $y_+ < 80$ .

As far as we know this is the first evidence of an objective time scale identified in the channel configuration. The time scale did not appear to be affected by spatial variability: it did not depend on the spanwise extent (different domain widths were considered) or the streamwise extent of the domain (two domains of different streamwise sizes were compared). We note that the dominant frequency of the nonlinear terms (e.g., the Reynolds stresses) should be on the order of 100-150 wall units. An interesting connection, which will need further exploration, can be made with wall reduction control schemes based on wall spanwise oscillations such as those of Quadrizio & Ricco (2004) and Choi *et al.* (1998), where it was shown that the optimal oscillation period is about 100-150 wall units.

The predominance of the characteristic frequency  $\bar{f}_{c+}$  at  $\bar{f}_+ = 0.0044$  is confirmed by Table 3, which shows the top 30 eigenvalues (denoted by  $\lambda_{l k f}^n$ ) with the corresponding Fourier mode indices  $(l, k, f)$  in space and time and quantum mode  $n$  for the configuration D3. Although a large fraction (18 modes) of the first 30 modes are associated to  $f \leq 2$ , which corresponds to long time scales that are outside the scope of our analysis, all the other modes are characterized by frequencies between 11 and 15, which correspond to the previously identified time scale of about 200-300 viscous units. The most energetic of these modes corresponds to  $f = 13$ , i.e.,  $\bar{f}_{c+}$ . We note that all the modes in the table are characterized by  $n = 1$ , which corresponds to the largest eigenvalue for a triad  $(l, k, f)$ , and  $l = 0$ , which corresponds to the streamwise-averaged flow.

To provide a comparison with standard analysis tools, Figures 4a and b show the temporal Fourier transform of the streamwise velocity component averaged along horizontal directions for two different heights:  $y_+ = 3$  and 15. Both spectra show, although not distinctly, a peak around the characteristic frequency  $\bar{f}_{c+}$ . This illustrates the usefulness of the new POD implementation.

Figures 5a and 5b respectively show the distribution of the top 5000 eigenvalues along  $\bar{k}_+$  and  $\bar{f}_+$  for the D3 configuration. Each eigenvalue is represented by a dot. Both figures show that the peaks observed in frequency and wavenumber space are not created by an accumulation of small eigenvalues, but correspond to coherent, more energetic structures. We note that Figure 5b also shows smaller, but noticeable peaks of  $\bar{f}_+$  at around 0.009 and 0.0135, which correspond to the harmonics of the frequency 0.0044.

Figure 6a shows that the energy spectrum integrated in frequency space  $\sum_f \lambda_{l k f}^1$  slowly decreases in an apparently self-similar manner with respect to both streamwise and spanwise wavenumbers. Figure 6b shows the corresponding variations in the frequency

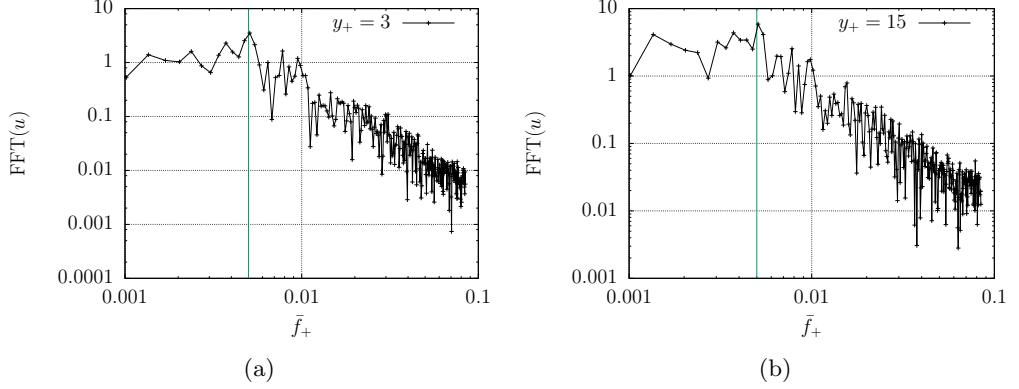


Figure 4: Horizontally-averaged ( $x$  and  $z$ ) temporal Fourier transform of the streamwise velocity component  $u$  as a function of  $\bar{f}_+$  in a log-log scale at a)  $y_+ = 3$  and b)  $y_+ = 15$ . A vertical line is shown at  $\bar{f}_+ = 0.005$  to indicate the peak in both figures.

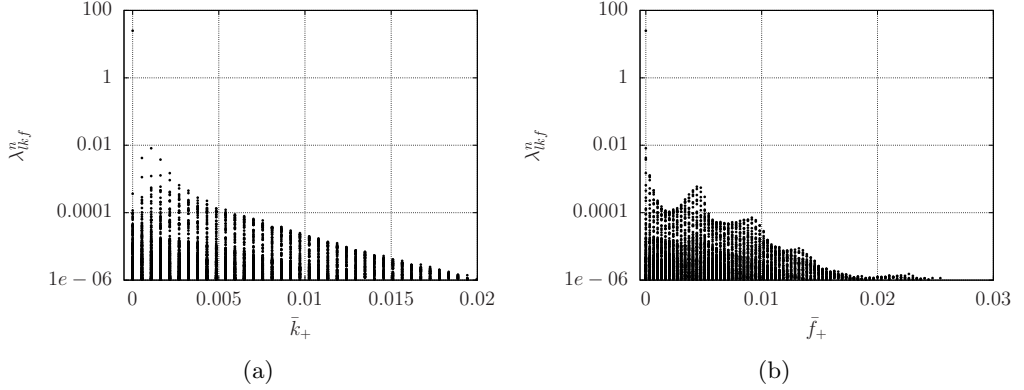


Figure 5: Eigenvalue distribution of the top 5000 eigenvalues for D3 configuration as a function of a)  $\bar{f}_+$  and b)  $\bar{k}_+$ .

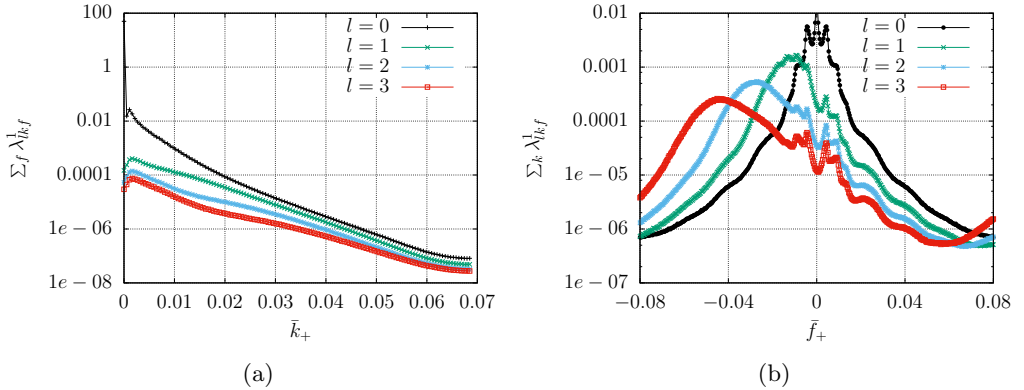


Figure 6: a) Energy spectrum summed over frequency  $f$ ,  $\sum_f \lambda_{lkf}^1$ , for different streamwise wavenumbers  $l$  as a function of  $\bar{k}_+$ . b) Energy spectrum summed over spanwise wavenumber  $k$ ,  $\sum_k \lambda_{lkf}^1$ , for different streamwise wavenumbers  $l$  as a function of  $\bar{f}_+$ .

---

$N$	$l$	$k$	$f$	$n$	$\lambda_{lkf}^n$	$N$	$l$	$k$	$f$	$n$	$\lambda_{lkf}^n$
1	0	0	0	1	24.97645	16	0	3	2	1	0.0004568
2	0	2	0	1	0.008133	17	0	2	2	1	0.0004559
3	0	1	0	1	0.004205	18	0	6	0	1	0.000451
4	0	3	0	1	0.003754	19	0	4	12	1	0.000415
5	0	4	0	1	0.001489	20	0	3	14	1	0.000412
6	0	3	1	1	0.001277	21	0	4	2	1	0.000396
7	0	2	1	1	0.001222	22	0	6	1	1	0.0003806
8	0	1	1	1	0.001128	23	0	0	1	1	0.0003643
9	0	4	1	1	0.000923	24	0	5	2	1	0.000349
10	0	5	0	1	0.000655	25	0	4	11	1	0.0003475
11	0	3	13	1	0.000591	26	0	2	12	1	0.0003445
12	0	2	14	1	0.000552	27	0	4	13	1	0.000335
13	0	5	0	1	0.000523	28	0	5	12	1	0.000314
14	0	2	13	1	0.000505	29	0	2	15	1	0.000295
15	0	3	12	1	0.000457	30	0	1	14	1	0.000289

---

Table 3: Top 30 most energetic eigenvalues  $\lambda_{lkf}^n$  along with their corresponding  $(l, k, f, n)$ .

space of the energy spectrum integrated in the spanwise wavenumber space for different streamwise wavenumbers  $l$ . For the  $l = 0$  mode, owing to spanwise reflection invariance, the plot is symmetric in the frequency space, and the characteristic frequency  $\bar{f}_{c+}$  and its harmonics can be clearly identified. These peaks observed at  $l = 0$  are still present in the  $l \neq 0$  spectra, which confirms that the characteristic frequency  $f_{c+}$  is not an artifact of the streamwise average. However non-zero streamwise wavenumbers are also characterized by a broad peak, which represents convection effects. In general, defining a convection velocity for the turbulent wall layer is not straightforward (Krogstad *et al.* (1998); Alamo & Jimenez (2009)), but the question can be more easily addressed in the present framework where each POD eigenfunction is naturally associated with a phase velocity  $-\bar{f}/\bar{l}$ . The spectra  $\sum_k \lambda_{lkf}^1$  can be used to define a global convection velocity  $c$  at each streamwise wavenumber using

$$c(\bar{l}) = -\frac{\bar{f}_{\max}}{\bar{l}}, \quad (4.2)$$

where

$$\bar{f}_{\max} = \arg \max_{\bar{f}} \left[ \sum_k \lambda_{lkf}^1 \right]. \quad (4.3)$$

Peaks in the spectra are located at  $\bar{f}_+ = (0.013, 0.027, 0.044)$  for respective streamwise wavenumbers of  $\bar{l}_+ = (0.0011, 0.0022, 0.0033)$ . This corresponds to a global convection velocity of  $12u_\tau$ , with a slight upward shift observed with increasing streamwise wavenumbers. This agrees well with the classical results (Kreplin & Eckelmann (1979), Krogstad *et al.* (1998), Wallace (2014), Alamo & Jimenez (2009)).

Having access to the four-dimensional space provides a way to test the Taylor's frozen turbulence hypothesis (Lumley 1965), which states that the spatial spectrum in the streamwise direction  $E_{k_x}$  of  $u(x)u(x')$  (where the overbar represents a spatial average) can be recovered from the temporal spectrum  $E_{\bar{f}}$  of  $\overline{u(t)u(t')}$  (the double overbar denotes here a temporal average) where  $\bar{f} = kU$  and  $U$  is a suitable convection velocity. In the context of the present decomposition, this leads us to compare, for each spanwise

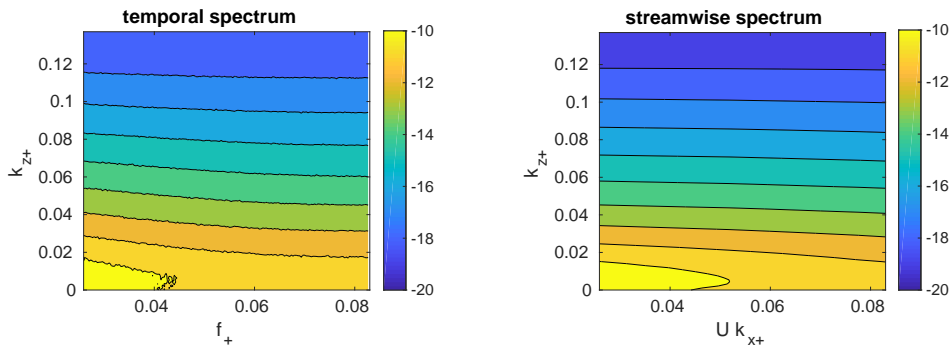


Figure 7: left: Eigenvalue spectrum  $\sum_l \lambda_{lkf}^1 \delta k_{x+}$  as a function of  $f_+$  ; right: Eigenvalue spectrum  $\sum_f \lambda_{lkf}^1 \delta k_{x+}$  as a function of  $k_{x+} U_{c+}$ , where  $U_{c+} = U = 12$ .

wavenumber  $k_z$  and quantum mode  $n$ , the temporal spectrum

$$\tilde{E}(\bar{f}, k_z, n) = \sum_l \lambda_{lkf}^n \delta k_x,$$

where  $\bar{f} = f/T$  and  $k_z = k/L_z$ , with the streamwise spectrum for the streamwise wavenumber  $k_x$

$$E(k_x, k_z, n) = \sum_f \lambda_{lkf}^n \delta \bar{f},$$

where  $k_x = l/L_x$ , using a suitable rescaling factor  $\delta k_x / \delta \bar{f}$  which can be obtained from

$$\mathcal{E} = \sum_l \sum_k \sum_f \lambda_{lkf}^1 \delta k_x \delta k_z \delta \bar{f} = \sum_l \sum_k E(k_x, k_z, n) \delta k_x \delta k_z = \sum_f \sum_k \tilde{E}(f, k_z, n) \delta \bar{f} \delta k_z.$$

For the first quantum mode  $n = 1$ , Figure 7 compares the spectra in the temporal direction  $E(k_x, k_z, 1)$  with the equivalent spectrum in the streamwise direction  $\tilde{E}(f, k_z, 1)$ . The frequency expressed in wall units  $f_+$  is related to the streamwise wavenumber  $k_{x+}$  such that  $k_{x+} U_{c+} = f_+$  where we have taken  $U_{c+} = 12$ . For the range of corresponding frequencies, a good agreement can be observed between the spectra at each spanwise wavenumber  $k_z$ .

#### 4.2. POD eigenfunctions

Figure 8 shows that the reconstructed mean streamwise profile coincides with previous results (Moser *et al.* (1999)) and with the dominant mode ( $l = 0, k = 0, f = 0, n = 1$ ) of the decomposition. Figure 9 shows the absolute value of each component of the most energetic mode  $\phi_{lkf}^{p,n}$ , for  $(\bar{l}_+, \bar{k}_+, \bar{f}_+) = (0, 0.0016, 0.0044)$ , obtained for the datasets D1-D3. As expected, there is a good agreement between the different configurations, which indicates convergence of the procedure at least for the most energetic modes. In all that follows only results for D3 and D4 will be presented.

In order to gain more insight on the structure of the modes, Figures 10a, c and e show the shape of the most energetic eigenfunction components  $\phi_{0kf}^{1,p}$  associated with the characteristic frequency  $\bar{f}_{c+} \sim 0.0044$  for different spanwise wavenumbers. The location of the velocity maxima moves closer to the wall as the spanwise wavenumber increases, which is in agreement with previous descriptions of wall-attached structures (Alamo *et al.* (2006), Podvin *et al.* (2010)). The values of the maxima are similar for both cross-stream components, also in agreement with previous observations (Alamo *et al.* (2006),

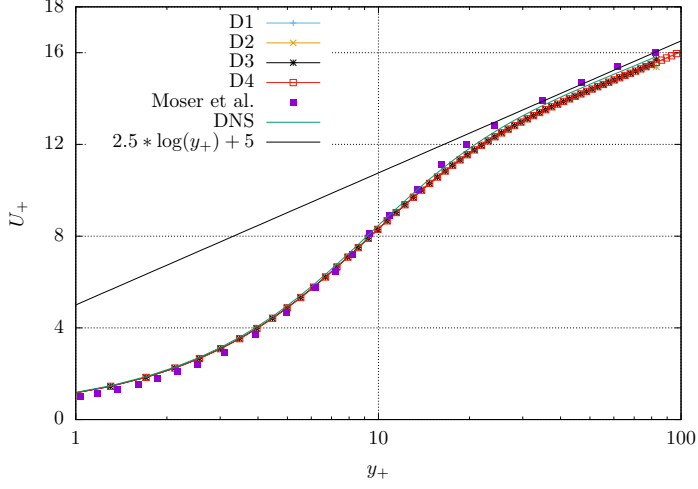
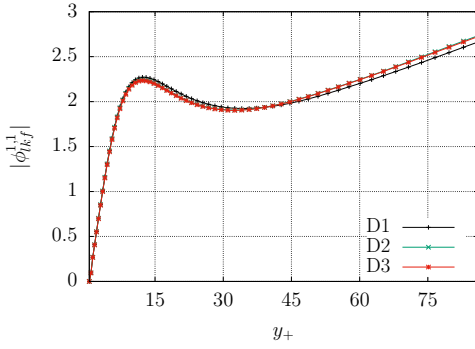
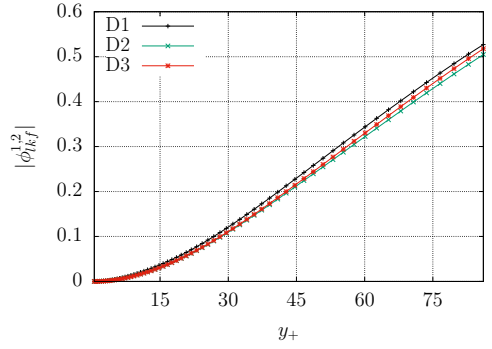


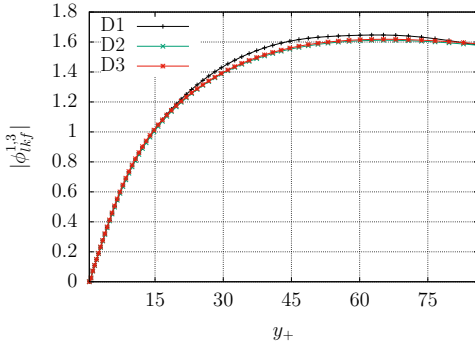
Figure 8: Comparison of the mean streamwise profile reconstructed using the first eigenfunction for the mode pair  $(0,0,0)$  with that of Moser *et al.* (1999), and with the mean profile obtained from the DNS.



(a) streamwise component



(b) wall-normal component



(c) spanwise component

Figure 9: Comparison of the eigenfunctions  $\phi_{l k f}^1$  corresponding to  $\bar{l}_+ = 0$ ,  $\bar{k}_+ = 0.0065$ ,  $\bar{f}_+ = 0.0044$  for different configurations.

Podvin & Fraigneau (2017)), but the value tends to increase with the spanwise wavenumber for the streamwise and the wall-normal component, while it slightly decreases for the spanwise component. The monotonous evolution of the shape of the modes with the spanwise wavenumber suggests self-similarity, as was proposed in Podvin & Fraigneau (2017).

Figures 10b, d and f compare the eigenfunctions obtained on the domain  $0 < y_+ < 80$  (for D3) and  $0 < y_+ < 590$  (for D4) for several spanwise wavenumbers. The eigenfunctions of D4 have been rescaled to have the same energy content as those of D3 on  $0 < y_+ < 80$ . We observe that the eigenfunctions nearly coincide over their common definition domain, which is not a trivial result. The persistence of the eigenfunction shape with respect to the wall-normal extension of the decomposition domain shows the coherence of the most energetic motions over the entire height of the boundary layer. It also means that the restrictions of the eigenfunctions on the larger domain are orthogonal to each other on the smaller domain (since they coincide with the eigenfunctions there), which makes it possible to recover the amplitude of the eigenfunction on the larger domain directly from the projection of the velocity field in the smaller domain onto the corresponding eigenfunction. This shows the relevance of the decomposition for estimation purposes in a context of partial information (see for instance Podvin *et al.* (2010)).

Figure 11 shows the hierarchical organization of the eigenfunctions in various dimensions of the four-dimensional space. For each streamwise wavenumber and quantum mode, we define the intensity of the eigenfunctions as a function of height and absolute frequency (for the sake of clarity positive and negative frequencies are aggregated, although as seen in a previous section there is no symmetry):  $I_{ln}(y, |\bar{f}|) = \sum_k (\lambda_{lkf}^n |\phi_{lkf}^n(y)|^2 + \lambda_{lk-f}^n |\phi_{lk-f}^n(y)|^2)$ . It is represented in Figure 11 for the first quantum numbers  $n \leq 4$  and selected streamwise wavenumbers  $l$ . Each quantum number  $n$  is characterized by  $n$  peaks at a given frequency. The wall-normal location of the highest peak increases nearly linearly with the quantum number  $n$ , and is about  $10n$  in wall units. At a given wavenumber in the horizontal space, energy is therefore transferred from the more energetic to the less energetic modes towards the core region away from the wall. The range of frequencies associated with a high intensity increases only slightly with the quantum number  $n$ , but increases significantly with the streamwise wavenumber  $l$  with a shift towards higher frequencies, which is due to convection effects.

Figure 12 shows the flow generated by selected modes in figure 10 associated with  $\bar{f}_{c+}$  for two different values of  $\bar{k}_+$ . As these dominant modes have no streamwise variation (i.e.,  $l = 0$ ), the three-dimensional shapes of the modes are represented by a contour plot of the streamwise velocity component ( $u$ ) and a velocity plot of the in-plane quantities ( $v, w$ ). The modes are characterized by updrafts of low-speed fluid alternating with downdrafts of high-speed fluid, associated with vortical motions in the streamwise direction, in agreement with classic observations (Corino & Brodkey 1969). The wall-normal extension of the structure decreases as the spanwise wavenumber increases, in agreement with Townsend's model (Townsend 1976) of wall-attached eddies (note the similarity of Figure 12 with Figure 9 in Jiménez (2013)). Figure 13 shows that the most energetic streamwise mode convected at a velocity of  $12u_\tau$  also corresponds to high and low-speed streaks alternating in the streamwise as well as in the spanwise direction and associated with vortical motions in the cross-stream plane. The wall-normal position of the vortex centers depends on the vertical extension of the streaks.

The contribution of the  $M$  most energetic modes to the fluctuating stresses can be

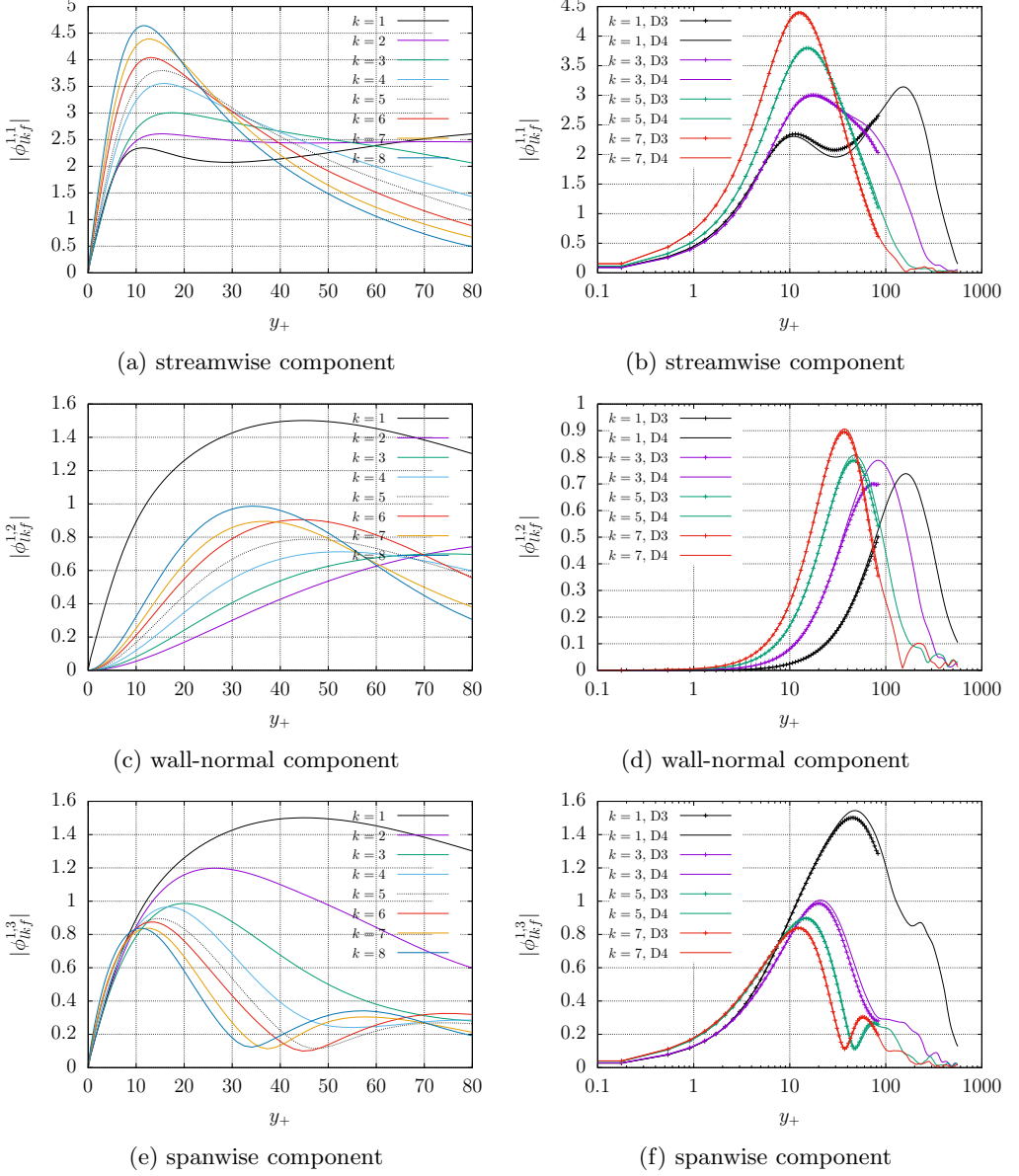


Figure 10: Dominant eigenfunctions  $\phi_{0kf}^1$  corresponding to  $\bar{f}_{c+}$  and for increasing values of  $\bar{k}_+$ . Top row: Streamwise component; Middle row: Wall-normal component; Bottom Row: Spanwise component; Left column: Comparison for  $0 < y_+ < 80$  (D3) and different spanwise wavenumbers ( $k = 1$  to  $8$  which corresponds to  $\bar{k}_+$  between  $0.0011$  to  $0.0086$ ); Right column: Comparison between the domains  $0 < y_+ < 80$  (D3) and  $0 < y_+ < 590$  (D4) for selected wavenumbers  $k = 1, 3, 5, 7$ .

evaluated using

$$\langle \overline{u^i u^j} \rangle_M = \sum_{N(l,k,f,n) \leq M} \lambda_{lkf}^n \phi_{lkf}^{n,*i} \phi_{lkf}^{m,j}, \quad (4.4)$$

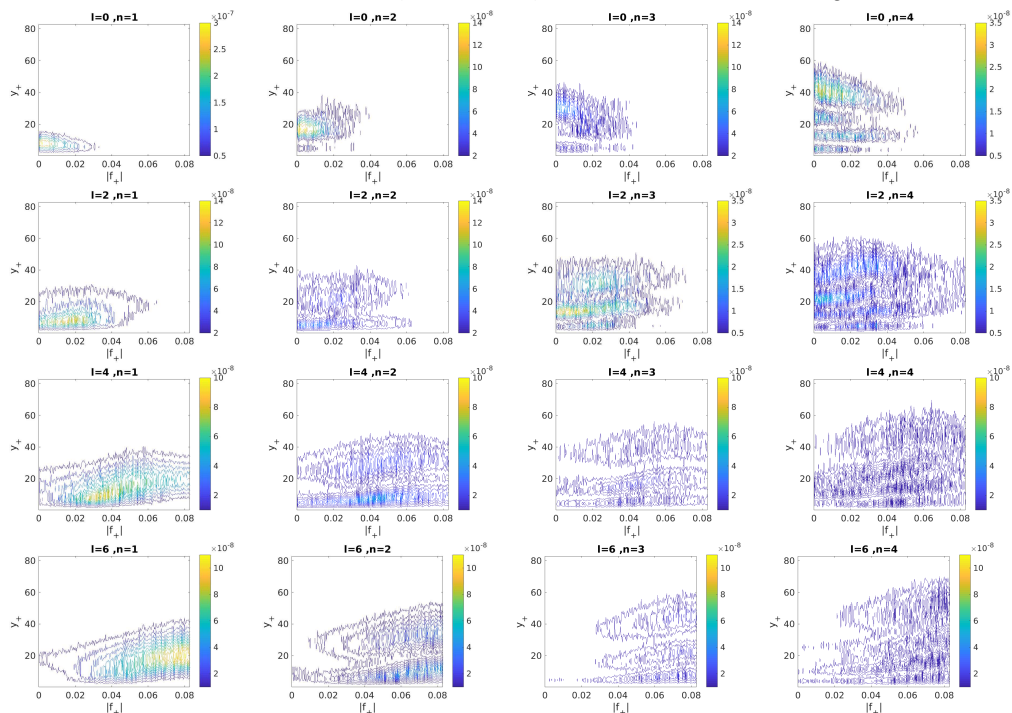


Figure 11: Structure intensity  $I_{ln}(y, |\bar{f}|) = \sum_k \lambda_{lkf}^n |\phi_{lkf}^n(y)|^2 + \lambda_{lk-f}^n |\phi_{lk-f}^n(y)|^2$  as a function of the vertical direction  $y$  and of the frequency  $|\bar{f}|$  for the first quantum numbers  $n \leq 4$  and different streamwise wavenumbers  $l$ . From left to right: increasing quantum numbers  $n = 1, 2, 3, 4$ . From top to bottom: increasing streamwise wavenumbers  $l = 0, 2, 4, 6$ .

where the subscript ‘ $M$ ’ is used to distinguish it as a reconstructed quantity using  $M$  most energetic modes. The bar indicates average over space and time and  $\langle \cdot \rangle$  denotes the usual ensemble operator. Note that the mean modes corresponding to  $(0, 0, 0, n)$  have been excluded from the reconstruction as the stresses are associated with fluctuating components. Figures 14a, b and c show the three components of the root-mean square velocity (rms) and Figure 14d shows the Reynolds stress as a function of  $y_+$  reconstructed using 200 and then 3000 modes. The plots are compared with the present simulation results and the DNS results of Moser *et al.* (1999). A non-negligible fraction of the turbulent intensity is recovered with the most energetic 200 modes: 60% for the streamwise velocity, 30% for the cross-stream components, and about 25% of the Reynolds stresses. The gain obtained using 15 times as many modes (3000) is relatively small (40% increase for the spanwise component and 30% for the wall-normal component), which highlights the complexity of the flow.

## 5. Energetics of modes

It is of interest to determine the contributions made by the most energetic POD modes to the momentum equations. In pioneering studies, Hong & Rubesin (1985) and Gatski & Glauser (1992) examined the contributions of the dominant POD mode. Hong and Rubesin showed that the dominant fluctuating mode captured several essential

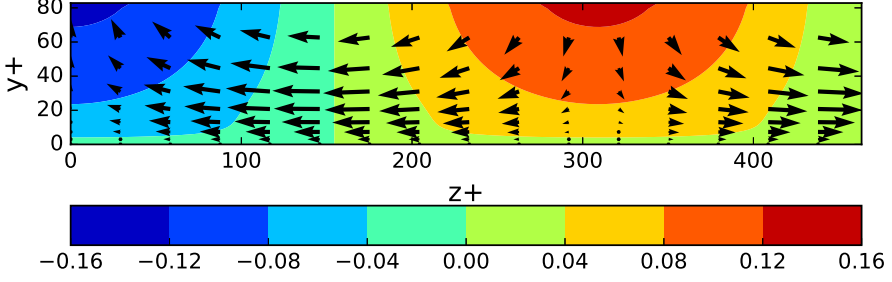
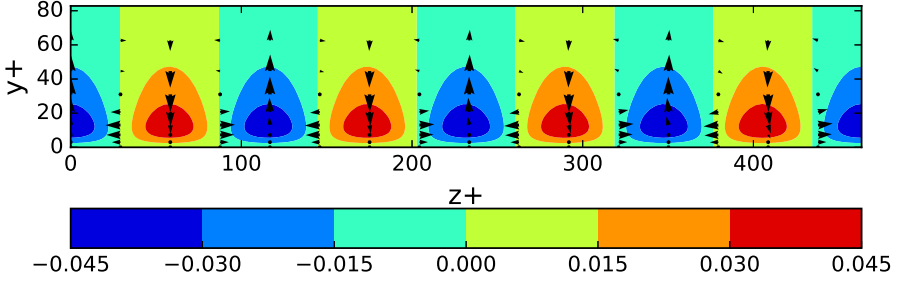
a)  $l = 0, k = 3, f = 13$ b)  $l = 0, k = 16, f = 13$ 

Figure 12: Contour plot of streamwise velocity component reconstructed from eigenfunction in  $(z, y)$  plane along with a vector plot for  $(w, v)$  velocity components for the non-trivial dominant eigenmode corresponding to a)  $l = 0, k = 3, f = 13, n = 1$  and b)  $l = 0, k = 16, f = 13, n = 1$ .

characteristics of the fully turbulent flow. Gatski and Glauser considered the various contributions of the first POD eigenmode to the different terms of the momentum equation and showed that a turbulent model for the transport term could be built from one-mode estimates.

With the new variant of Proper Orthogonal Decomposition, projection of the Navier-Stokes equations onto the basis of eigenfunctions no longer yields a dynamical system for the temporal amplitudes of the spatial eigenfunctions, but makes it possible to evaluate the contributions made by the different terms of the momentum equations for each mode  $N(l, k, f, n)$ .

For consistency with standard analysis, we decompose the  $p$ th component of the

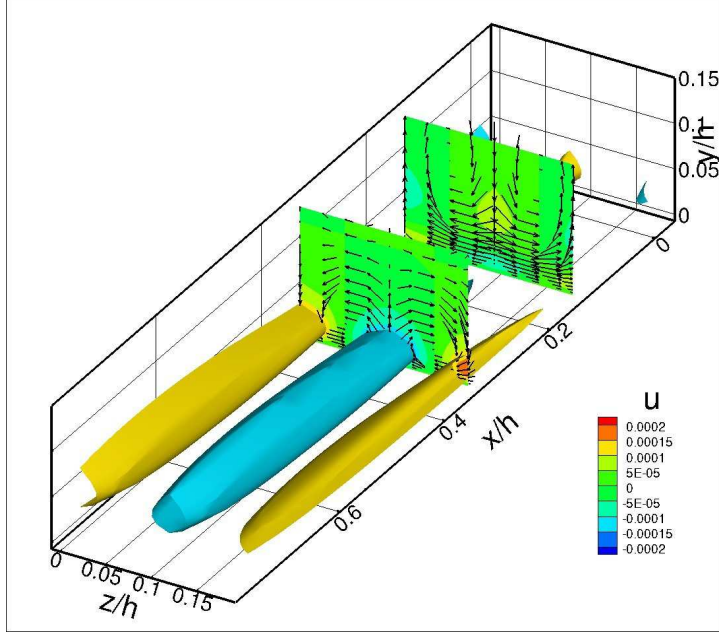


Figure 13: Reconstruction of the most energetic mode corresponding to the peak in the frequency spectrum in figure 6b for  $l = 1$ ,  $k = 16$ ,  $f = -40$ ,  $n = 1$ . Isosurfaces (in arbitrary units) of streamwise component in  $(x, y, z)$  are shown along with two slice views at  $x/h = 0.15$  and  $x/h = 0.35$  showing a contour plot of the streamwise component and a vector plot of the spanwise and wall-normal components.

velocity field into its mean part  $U^p$  which, as we have seen above, can be represented by the mode  $(0, 0, 0, 1)$  and a fluctuating part  $u^p$ .

We rewrite the equations as

$$E_p = -\frac{\partial u^p}{\partial t} - u^j \frac{\partial U^p}{\partial x_j} - U^j \frac{\partial u^p}{\partial x_j} - u^j \frac{\partial u^p}{\partial x_j} - \frac{\partial p}{\partial x_p} + \nu \frac{\partial^2 u^p}{\partial x_j \partial x_j} = 0, \quad (5.1)$$

where  $U^1 = U$  (mean streamwise velocity) and  $U^j = 0$  if  $j = 2, 3$  and  $\frac{\partial U^p}{\partial x_j} \neq 0$  only if  $p = 1$  and  $j = 2$ .

To obtain a budget for each mode  $(l, k, f, n)$  we project Equation (5.1) onto the corresponding mode, i.e., we take the Fourier transform in the  $(l, k, f)$  space, take the inner product in the wall-normal direction, and apply an ensemble average. This gives

$$\int_0^{L_x} \int_0^{L_z} \int_0^T \int_0^Y \langle E_p a_{lkf}^{*n} \rangle \phi_{lkf}^{*n,p}(y) e^{-2\pi i(lx/L_x + kz/L_z + ft/T)} dy dt dz dx, \quad (5.2)$$

where  $*$  denotes complex conjugation.

- The first term  $-\frac{\partial u^p}{\partial t}$  yields a contribution  $-I_{lkf}^n = -i\bar{f}\lambda_{lkf}^n$ . We note that this contribution is purely imaginary.

- The second and third terms represent the interaction of the mode with the mean velocity profile. The second term is associated with the classic production term and is expected to represent a source of energy for the fluctuations:

$$P_{lkf}^n = -\int_0^Y \left\langle u^2 \frac{dU}{dy} a_{lkf}^{*n} \phi_{lkf}^{*n,1} \right\rangle dy = -\lambda_{lkf}^n \int_0^Y \frac{dU}{dy} \phi_{lkf}^{n,2} \phi_{lkf}^{*n,1} dy. \quad (5.3)$$

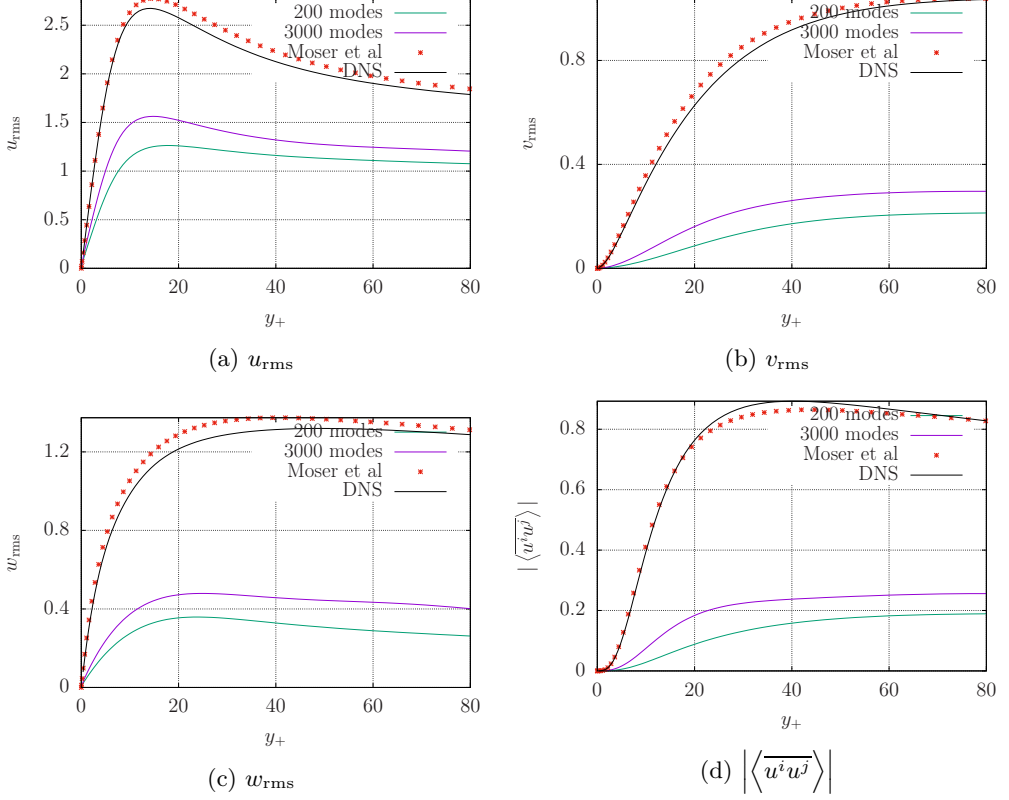


Figure 14: Reconstruction of the turbulent intensities and Reynolds stress using 200 and 3000 modes. Comparison with Moser *et al.* (1999)'s and our DNS data is also shown.

The third term represents the convection effect of the mean field:

$$\begin{aligned}
 C_{lkf}^n &= - \int_0^Y \left\langle U \frac{\partial u^p}{\partial x_1} a_{lkf}^{*n,p} \phi_{lkf}^{*n,p} \right\rangle dy = - \int_0^Y \sum_m U \frac{\partial \phi_{lkf}^{m,p}}{\partial x_1} \phi_{lkf}^{*n,p} \langle a_{lkf}^m a_{lkf}^{*n} \rangle dy \\
 &= -i\bar{l}\lambda_{lkf}^n \int_0^Y U \phi_{lkf}^{n,p} \phi_{lkf}^{*n,p} dy.
 \end{aligned} \tag{5.4}$$

• The last term on the left-hand-side of the equation corresponds to the viscous diffusion term  $D_{lkf}^n$  defined as:

$$D_{lkf}^n = \lambda_{lkf}^n \int_0^Y \frac{\partial^2 \phi_{lkf}^{n,p}}{\partial x_j \partial x_j} \phi_{lkf}^{*n,p} dy = \lambda_{lkf}^n \left[ (-\bar{l}^2 - \bar{k}^2) \int_0^Y \phi_{lkf}^{n,p} \phi_{lkf}^{*n,p} dy + \int_0^Y \frac{d^2 \phi_{lkf}^{n,p}}{dy^2} \phi_{lkf}^{*n,p} dy \right]. \tag{5.5}$$

Integrating the last term by parts, one has

$$D_{lkf}^n = (-\bar{l}^2 - \bar{k}^2) - \int_0^Y \frac{d\phi_{lkf}^{n,p}}{dy} \frac{d\phi_{lkf}^{*n,p}}{dy} dy + \frac{d\phi_{lkf}^{n,i}(Y)}{dy} \phi_{lkf}^{*n,i}(Y). \tag{5.6}$$

Except for the last term corresponding to a boundary effect, all contributions to  $D_{lkf}^n$  are real and negative, which corresponds to an energy loss for the mode, as expected. Note that  $I_{lkf}^n, P_{lkf}^n, C_{lkf}^n$  and  $D_{lkf}^n$  only require information about the mode  $(l, k, f, n)$

(one can think of them as purely diagonal operators) and can be directly evaluated from the Proper Orthogonal Decomposition, while the other two contributions require additional information about the coefficients  $a_{lkf}^n$ .

- As in the classic derivation (Aubry *et al.* (1988)), the contribution from the pressure term represents the influence of the pressure at the upper boundary of the wall layer and can be expressed as

$$Pr_{lkf}^n = \langle p_{lkf}(Y) a_{lkf}^{*n} \rangle \phi_{lkf}^{*n,2}(Y),$$

where  $p_{lkf}(Y)$  is the Fourier transform (along  $x$ ,  $z$  and  $t$ ) of pressure at height  $Y$ , which needs to be evaluated from the DNS. This term is proportional to the wall-normal intensity of the structure at the top of the layer and depends on the velocity-pressure correlation at the top of the layer. It represents an external forcing term which corresponds to the interaction of the wall layer with the outer region (Aubry *et al.* 1988).

- Finally, the quadratic interactions can be evaluated as

$$Q_{lkf}^n = - \sum_{l'} \sum_{k'} \sum_{f'} \sum_m \sum_p \left\langle a_{l'k'f'}^m a_{l-l'k-k'f-f'}^p a_{lkf}^{*n} \right\rangle \int_0^Y \frac{\partial \phi_{l'k'f'}^{m,i}}{\partial x_j} \phi_{l-l'k-k'f-f'}^{p,j} \phi_{lkf}^{*n,i} dy. \quad (5.7)$$

$Q_{lkf}^n$  requires information about the triple correlations of the coefficients  $a_{lkf}^n$ , and involves first derivatives of the eigenfunctions. This term characterizes the energy transfer from the different modes to the mode  $(l, k, f, n)$ . It can be seen as a non-isotropic extension of the energy transfer function defined in isotropic turbulence (Zhou 1993), and involves triads of modes in the  $(l, k, f)$  space. It also corresponds to the forcing term of the resolvent analysis (McKeon 2017).

If all other terms are known, the quadratic interaction terms  $Q_{lkf}^n$  can be determined from the budget equation:

$$I_{lkf}^n = P_{lkf}^n + C_{lkf}^n + D_{lkf}^n + Pr_{lkf}^n + Q_{lkf}^n. \quad (5.8)$$

The real part of the equation represents a balance between the production  $P_{lkf}^n$  and dissipation term  $D_{lkf}^n$ , which depend only on the characteristics of the mode  $(l, k, f, n)$ , and the interaction terms due to pressure  $Pr_{lkf}^n$  and convection by velocity fluctuations  $Q_{lkf}^n$ , which characterize how the mode interacts with the full flow. The imaginary part of the equation can be seen as a phase dispersion relation linking the frequency  $f$  of the mode ( $I_{lkf}^n$ ) with the different physical mechanisms.

Figure 15 represents the contributions of the different terms to the equations for the largest 200 modes (the contributions of the modes corresponding to the mean flow were set to zero). These modes are all characterized by a zero streamwise wavenumber ( $l = 0$ ) and a quantum number  $n = 1$ . All terms are evaluated directly, except the quadratic term  $Q_{0kf}^1$  which is evaluated using Equation (5.8). We have checked (not shown here though) that the quadratic terms could not be evaluated correctly by direct computation limited to the first 200 modes, as higher-order contributions were significant, which is typical of the closure problem.

For the sake of clarity, the left plots show mode number  $N$  from 1 – 30 and the right plots show  $N$  from 30 – 200. The top row (Figures 15a and b) shows that the real part of the production term  $P_{lkf}^n$  is essentially balanced by the sum of the real part of the dissipation and the quadratic terms. For the less energetic modes  $N > 30$  (Figure 15b) we note that the quadratic terms are mostly negative, which is consistent with the idea of a positive energy transfer from the large scales (most energetic modes) to the small scales. Figure 15 shows that the pressure interaction term is very small compared to the other terms, in agreement with Aubry *et al.* (1988)'s derivation where it is modeled as

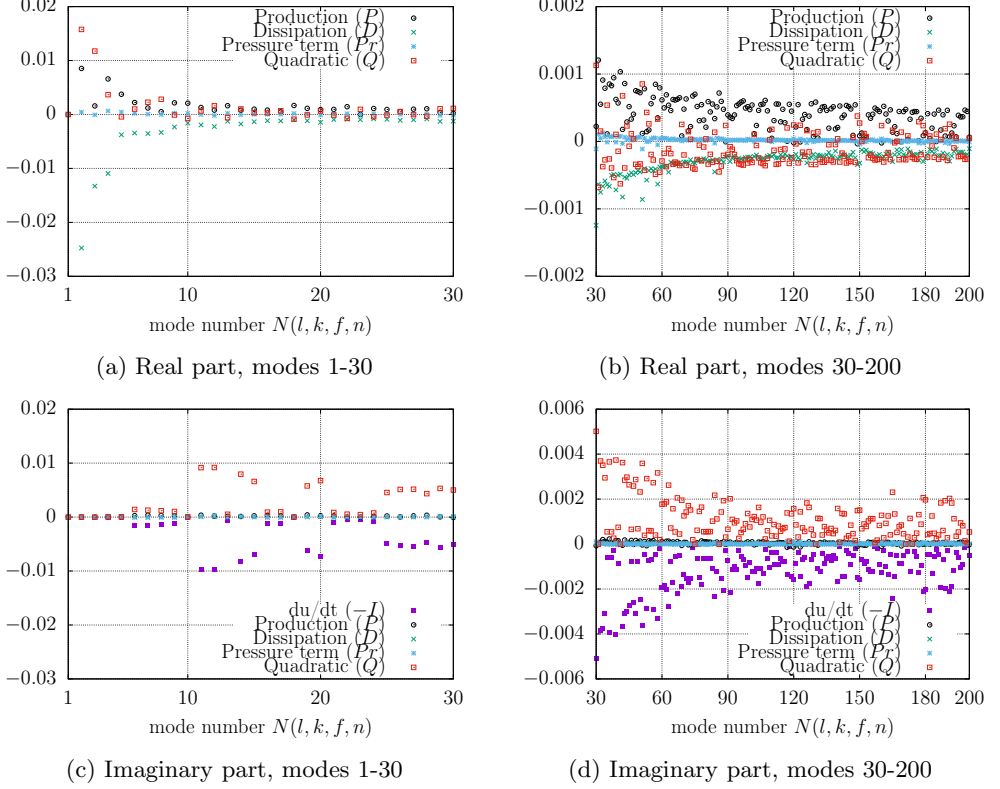


Figure 15: Energy budget for the first 200 most energetic spatially fluctuating modes.

a stochastic term of small amplitude. If we neglect the influence of the pressure term we have

$$-\text{Re}[Q_{0kf}^1] \sim P_{0kf}^1 + D_{0kf}^1. \quad (5.9)$$

Figures 15c and d show that for the most energetic modes, as  $l = 0$ , the frequency  $f$  of the mode is directly related to the imaginary part (denoted by  $\text{Im}$ ) of the nonlinear contributions to the mode  $(l, k, f, n)$ :

$$\text{Im}[Q_{0kf}^1] \sim i\bar{f}\lambda_{0kf}^n. \quad (5.10)$$

This corresponds to the following closure approximation:

$$\begin{aligned} -Q_{0kf}^1 &\sim \sum_{l'} \sum_{k'} \sum_{f'} \sum_m \sum_p \left[ \left\langle a_{l'k'f'}^m a_{l-l'k-k'f-f'}^p a_{0kf}^{*n} \right\rangle \int \frac{\partial \phi_{l'k'f'}^{m,i}}{\partial x_j} \phi_{l-l'k-k'f-f'}^{p,j} \phi_{0kf}^{*1,i} dy \right] \\ &\sim P_{0kf}^1 + D_{0kf}^1 - i\bar{f}\lambda_{0kf}^1. \end{aligned} \quad (5.11)$$

As observed above, we can see that triple correlations between the different POD modes are essential to characterize the energy transfer between the scales. Computing these correlations is difficult, however if  $Q_{lkf}^n$  can be determined from Equation (5.8), the

decomposition offers a new way to reconstruct the quadratic terms using

$$-u^j \frac{\partial u^p}{\partial x_j} = \sum_l \sum_k \sum_f \sum_n \frac{a_{lkf}^n}{\lambda_{lkf}^n} Q_{lkf}^n \phi_{lkf}^{n,p}(y) e^{2\pi i(lx/L_x + kz/L_z + ft/T)} \quad (5.12)$$

Substitution of the velocity decomposition into the left-hand side of the equation requires performing a cumbersome convolution on all coefficients  $a_{lkf}^n$ , but the right-hand-side provides a straightforward expression of the quadratic terms in the stochastic POD basis of coefficients  $a_{lkf}^n$ , where coordinates are solely determined from second-order statistics. At each scale level  $(l, k, f, n)$ , the effect of the quadratic terms is to stretch and to rotate the corresponding velocity mode by a factor  $Q_{lkf}^n$ . Direct modeling of the distribution of  $a_{lkf}^n$  could therefore lead to new formulations of turbulence models in the decomposition framework.

## 6. Conclusion

Spatio-temporal Proper Orthogonal Decomposition has been applied to the wall layer of a turbulent channel flow. The decomposition represents an efficient data reduction technique which is adapted to large simulation databases. It brings to light typical features of wall turbulence in a straightforward manner, but also provides a fresh viewpoint on the flow organization. Due to symmetry properties, the decomposition singles out empirical eigenfunctions for each frequency and horizontal spatial wavenumber. Besides time scales superior to 3000 wall units, which our limited implementation of POD did not allow us to characterize fully, we have shown that the most energetic modes were characterized by a time scale on the order of 250 wall units, which could have significant implications for control. Convection velocities could be directly defined from the POD spectrum. A global convection velocity on the order of  $12u_\tau$  was identified in the wall layer, in good agreement with previous approaches. Examination of the spectrum provided some validation of the Taylor's frozen turbulence hypothesis.

About 30% of the turbulent kinetic energy was captured by the 200 most energetic modes. The most energetic modes were found to have a self-similar shape that appeared largely independent from the wall-normal extent of the decomposition domain, which shows the coherence of the motions over the height of the boundary layer. The modes appeared to be hierarchically organized, with a number of peaks and a maximal peak location at  $l = 0$  directly proportional to the quantum number  $n$ , indicating that energy cascading towards the higher-order modes is directed away from the wall into the core region.

Finally, substitution of the decomposition into the Navier-Stokes equation and numerical computation of the different contributions of the modes to the turbulent kinetic energy budget highlighted the key role played by quadratic interactions and allowed us to propose a new closure formulation to model the contribution of these interactions. Such relationships, which need to be further explored in a careful manner, could be useful to derive new turbulence models. We hope that this work will pave the way for comprehensive investigations of wall turbulent flows using spatio-temporal Proper Orthogonal Decomposition.

## Acknowledgements

We are grateful to W.K. George for motivating discussions. We thank the anonymous referees for pointing out valuable references and making helpful suggestions. This work

was supported by the Center of Data Science from the Paris-Saclay University. Computations were carried out at IDRIS-GENCI (project 02262).

## REFERENCES

- ALAMO, J. C. DEL & JIMENEZ, J. 2009 Estimation of turbulent convection velocities and corrections to Taylor's approximation. *Journal of Fluid Mechanics* **640**.
- ALAMO, J. C. DEL, JIMENEZ, J., ZANDONADE, P. & MOSER, R. D. 2006 Self-similar vortex clusters in the turbulent logarithmic region. *Journal of Fluid Mechanics* **561**.
- ARNDT, R.E.A., LONG, D.F. & GLAUSER, M.N. 1997 The proper orthogonal decomposition of pressure surrounding a turbulent jet. *J. Fluid Mech.* **340**, 1–33.
- AUBRY, N., HOLMES, P., LUMLEY, J. L. & STONE, E. 1988 The dynamics of coherent structures in the wall region of the wall boundary layer. *Journal of Fluid Mechanics* **192**.
- BLACKWELDER, R. F. & HARITODINIS, J. H. 1983 Scaling of the bursting frequency in turbulent boundary layers. *Journal of Fluid Mechanics* **132**.
- CHEN, K.K., TU, J.H. & ROWLEY, C.W. 2012 Variants of dynamic mode decomposition: boundary condition, koopman, and Fourier analyses. *J. Nonlinear Sci.* **22** (6), 887–915.
- CHOI, K.S., DEBISSCHOP, J.R. & CLAYTON, B.R. 1998 Turbulent boundary layer control by means of spanwise wall oscillations. *AIAA Journal* **36** (7), 1157–1163.
- CITRINITI, J. & GEORGE, W. 2000 Reconstruction of the global velocity field in the axisymmetric mixing layer utilizing the proper orthogonal decomposition. *J. Fluid Mech.* **418**, 137–166.
- CORINO, E. R. & BRODKEY, R. S. 1969 A visual investigation of the wall region in turbulent flow. *Journal of Fluid Mechanics* **37**.
- DELVILLE, J., UKEILEY, L., CORDIER, L., BONNET, J.P. & GLAUSER, M. 1999 Examination of large-scale structures in a turbulent plane mixing layer. part 1. proper orthogonal decomposition. *J. Fluid Mech.* **391**, 91–122.
- DENNIS, DAVID J.C. 2015 Coherent structures in wall-bounded turbulence. *Anais da Academia Brasileira de Ciencias* **87**, 1161 – 1193.
- FOUCART, S. & RAUHUT, H. 2013 *A mathematical introduction to compressive sensing*. New York: Birkhäuser/Springer.
- FRISCH, U. 1995 *Turbulence*. Cambridge University Press.
- GATSKI, M. & GLAUSER, M. 1992 Proper orthogonal decomposition based turbulence modeling. In *Instability, Transition and Turbulence* (ed. M.Y. Hussaini, A. Kumar & C.L. Streett). Springer.
- GEORGE, W. K. 2017 A 50-year retrospective and the future. In *Whither Turbulence and Big Data in the 21st Century?*. Springer.
- GLAUSER, M.N. & GEORGE, W.K. 1987 An orthogonal decomposition of the axisymmetric jet mixing layer utilizing cross-wire measurements. In *Proceedings of the Sixth Symposium on Turbulent Shear Flow*. Toulouse.
- GLAUSER, M.N., LEIB, S.J. & GEORGE, W.K. 1983 An application of Lumley's orthogonal decomposition to the axisymmetric jet mixing layer. In *Bulletin of American Physical Society*. DFD Meeting, Houston, Texas.
- HALKO, N., MARTINSSON, P.G. & TROPP, J.A. 2011 Finding structure with randomness: probabilistic algorithms for constructing approximate matrix decompositions. *SIAM Rev.* **53** (2), 217–288.
- HAMILTON, J. M., KIM, J. & WALEFFE, F. 1995 Regeneration mechanisms of near-wall turbulence structures. *Journal of Fluid Mechanics* **287**.
- HONG, S.K. & RUBESIN, M.W. 1985 Application of large-eddy interaction model to channel flow. *Tech. Rep.* 86691. NASA Technical Memorandum.
- JIMÉNEZ, J. 2013 Near-wall turbulence. *Physics of Fluids* **25** (10).
- JIMENEZ, J. & MOIN, P. 1991 The minimal flow unit in near-wall turbulence. *Journal of Fluid Mechanics* **225**.
- KANNAN, R. & VEMPALA, S. 2017 Randomized algorithms in numerical linear algebra. *Acta Numer.* **26**, 95–135.

- KIM, H. T., KLINE, S. J. & REYNOLDS, W. C. 1971 The production of turbulence near a smooth wall in a turbulent boundary layer. *Journal of Fluid Mechanics* **50** (1).
- KREPLIN, H. P. & ECKELMANN, H. 1979 Propagation of perturbations in the viscous sublayer and adjacent wall region. *Journal of Fluid Mechanics* **95**.
- KROGSTAD, P. A., KASPERSEN, J. H. & RINESTAD, S. 1998 Convection velocities in a turbulent boundary layer. *Physics of Fluids* **10**.
- LOÈVE, M. 1977 *Probability Theory*. Berlin, Germany: Springer.
- LUMLEY, J.L. 1965 On the interpretation of temporal spectra in high intensity shear flows. *Phys. Fluids* **8**, 1056.
- LUMLEY, J. L. 1967 The structure of inhomogeneous turbulent flows. In *Atmospheric Turbulence and Radio Wave Propagation*. Nauka, Moscow.
- MCKEON, B. J. 2017 The engine behind (wall) turbulence: perspectives on scale interactions. *Journal of Fluid Mechanics* **817**.
- MEZIĆ, I. 2005 Spectral properties of dynamical systems, model reduction and decompositions. *Nonlinear Dyn.* **41** (1), 309–325.
- MOIN, P. & MOSER, R. D. 1989 Characteristic-eddy decomposition of turbulence in a channel. *Journal of Fluid Mechanics* **200**.
- MOSER, R. D., KIM, J. & MANSOUR, N. N. 1999 Direct numerical simulation of turbulent channel flow up to  $Re_\tau = 590$ . *Physics of Fluids* **11** (4).
- PODVIN, B. 2001 On the adequacy of the ten-dimensional model for the wall layer. *Physics of Fluids* **13** (1).
- PODVIN, B. & FRAIGNEAU, Y. 2014 POD-based wall boundary conditions for the numerical simulation of turbulent channel flows. *Journal of Turbulence* **15** (3).
- PODVIN, B. & FRAIGNEAU, Y. 2017 A few thoughts on proper orthogonal decomposition in turbulence. *Physics of Fluids* **29**.
- PODVIN, B., FRAIGNEAU, Y., JOUANGUY, J. & LAVAL, J. P. 2010 On self-similarity in the inner wall layer of a turbulent channel flow. *Journal of Fluids Engineering* **132** (4).
- PODVIN, B. & LUMLEY, J. L. 1998 A low-dimensional approach for the minimal flow unit. *Journal of Fluid Mechanics* **362**.
- QUADRIZIO, M. & RICCO, P. 2004 Critical assessment of drag reduction through spanwise wall oscillations. *Journal of Fluid Mechanics* **521**, 251–271.
- ROBINSON, S. K. 1991 Coherent motions in the turbulent boundary layer. *Annual Review of Fluid Mechanics* **23**.
- ROWLEY, C.W., MEZIĆ, I., BAGHERI, S., SCHLATTER, P. & HENNINGSON, D.S. 2009 Spectral analysis of nonlinear flows. *J. Fluid Mech.* **641**, 115–127.
- SCHMID, P.J. 2010 Dynamic mode decomposition of numerical and experimental data. *J. Fluid Mech.* **656**, 5–28.
- SIROVICH, L. 1987 Turbulence and the dynamics of coherent structures. *Quart. J. Appl. Math.* **45**, 561–590.
- SMITS, A. J., MCKEON, B. J. & MARUSIC, I. 2011 High-reynolds number wall turbulence. *Annual Review of Fluid Mechanics* **43** (1).
- STANISLAS, M., JIMENEZ, J. & MARUSIC, I., ed. 2011 *Progress in Wall Turbulence: Understanding and Modeling*. Springer.
- STANISLAS, M., PERRET, L. & FOUCAUT, J. M. 2008 Vortical structures in the turbulent boundary layer: a possible route to a universal representation. *Journal of Fluid Mechanics* **602**.
- TIBSHIRANI, R. 1996 Regression shrinkage and selection via the lasso. *J. Royal Stat. Soc. Series B* **58** (1), 267–288.
- TOWNE, A., SCHMIDT, O. & COLONIUS, T. 2018 Spectral proper orthogonal decomposition and its relationship to dynamic mode decomposition and resolvent analysis. *J. Fluid Mech.* **847**, 821–867.
- TOWNSEND, A. A. 1976 *The Structure of turbulent shear flow*. Cambridge University Press.
- UKEILEY, L., CORDIER, L., MANCEAU, R., DELVILLE, J., GLAUSER, M. & BONNET, J. 2001 Examination of large- scale structures in a turbulent plane mixing layer. part 2. dynamical systems model. *J. Fluid Mech.* **441**, 67–108.
- WALLACE, J. M. 2014 Space-time correlations in turbulent flow: A review. *Theoretical and Applied Mechanics Letters* **4**.

- WESTERWHEEL, J., ELSINGA, G. E. & ADRIAN, R. J. 2013 Particle image velocimetry for complex and turbulent flows. *Ann. Review Fluid Mech.* **45**, 409–436.
- ZHOU, J. 1993 Interacting scales and energy transfer in isotropic turbulence. *Tech. Rep.* CR-191477. NASA.